STEREO SCIENCE RESULTS AT SOLAR MINIMUM

Reconstructing the 3D Morphology of the 17 May 2008 CME

**B.E. Wood · R.A. Howard · A. Thernisien ·
S.P. Plunkett · D.G. Socker**

Abstract We model the kinematics and three-dimensional distribution of mass in a coronal mass ejection (CME) observed on 17 May 2008, using a comprehensive analysis of STEREO images of the CME. The CME is a surprisingly fast one for solar minimum, reaching velocities of up to 1120 km s^{-1}. It can be followed continuously from inception all the way out to 1 AU. We find that the appearance of the CME can be modeled reasonably well as a combination of two distinct fronts that expand outward in a self-similar fashion. The model implies that STEREO-B is struck by the weaker of these two fronts on 19 May, and the *in situ* instruments on STEREO-B do see a weak density and magnetic field enhancement at the expected time.

Keywords Coronal mass ejections, initiation and propagation · Coronal mass ejections, interplanetary

1. Introduction

Interpretation of coronagraphic images of coronal mass ejections (CMEs) has always been complicated by difficulties in inferring their three-dimensional structure from two-dimensional data. The *Solar TErrestrial RElations Observatory* (STEREO) mission is intended to mitigate this problem in a couple of important ways. Most importantly, STEREO uses two separate spacecraft to observe CMEs from two very different vantage points, with one spacecraft (STEREO-A) orbiting the Sun ahead of the Earth and the other (STEREO-B) trailing behind. The idea is that simultaneous images of a CME from different locations should allow a better determination of how the observed mass is distributed in three-dimensional space.

B.E. Wood (✉) · R.A. Howard · A. Thernisien · S.P. Plunkett · D.G. Socker
Naval Research Laboratory, Space Science Division, Washington, DC 20375, USA
e-mail: brian.wood@nrl.navy.mil

A second characteristic of STEREO that is valuable for studying 3D CME structure is that each STEREO spacecraft carries a package of telescopes, collectively called the Sun-Earth Connection Coronal and Heliospheric Investigation (SECCHI), capable of continuously tracking CMEs from their initiation near the Sun, into the interplanetary medium (IPM), and all the way to 1 AU (Howard *et al.*, 2008; Harrison *et al.*, 2008; Wood *et al.*, 2009). During the long journey to 1 AU, each STEREO spacecraft by itself will view a CME from multiple perspectives. This is not the case for the instruments on the *Solar and Heliospheric Observatory* (SOHO), for example, which can only image CMEs relatively close to the Sun.

Although STEREO in principle provides the sort of comprehensive observations necessary to determine a CME's 3D mass distribution, there is no single best method that defines exactly how to get from the data to the reconstructed density distribution. The most objective approach is computational tomography, which involves simply feeding a tomographic reconstruction program simultaneous images of a CME from the two STEREO spacecraft, and then letting the program compute the most likely mass distribution (Antunes *et al.*, 2008; Antunes, Thernisien, and Yahil, 2009). However, two viewpoints may be insufficient for a clean, unambiguous tomographic reconstruction, and it is also difficult for this approach to simultaneously take into account constraints on CME structure provided by observations at different times.

Another approach is to rely on physical models of CME magnetic structures to guide interpretation of the CME images. In many of these models it is assumed that a magnetic flux rope topology is at the core of all CMEs. Such modeling has been used extensively in the analysis of SOHO observations (Chen *et al.*, 1997; Gibson and Low, 1998; Wu, Andrews, and Plunkett, 2001; Manchester *et al.*, 2004; Thernisien, Howard, and Vourlidas, 2006; Krall, 2007) and will surely be used in the analysis of STEREO data as well (Thernisien, Vourlidas, and Howard, 2009). However, it is clearly worthwhile to explore more empirical techniques that fully utilize the wealth of new observational constraints provided by STEREO, while remaining unconstrained by any theoretical preconceptions of what a CME should look like.

To this end, we here attempt to reconstruct the 3D mass distribution of a CME from 17 May 2008 using an intuitive trial-and-error method, where synthetic SECCHI images are computed from an assumed 3D density distribution, and then the distribution is repeatedly altered to obtain better and better visual agreement with the data. The strength of this simple approach is that it requires that the final 3D density cube containing the CME mass distribution simultaneously reproduce the appearance of the CME in *all* STEREO images of it – at all times and from both spacecraft. The analysis therefore makes full use of the extensive set of observational constraints provided by STEREO, though it is time consuming and somewhat subjective in nature.

2. The 17 May 2008 CME

Figure 1 shows the locations of the two STEREO spacecraft, STEREO-A and STEREO-B, on 17 May 2008, at which time the spacecraft separation was 51.7°. The positions are plotted in heliocentric aries ecliptic (HAE) coordinates, in which the ecliptic defines the xy-axes and the negative x-axis points toward the vernal equinox. At about 9:56 UT, the SECCHI/EUVI imagers on both spacecraft observe the beginnings of a flare, which also signals the initiation of the CME. In Figure 2, images are shown from EUVI's Fe XII λ195 bandpass. The flare is near the east limb as seen from STEREO-A, but it is very close to disk center as viewed
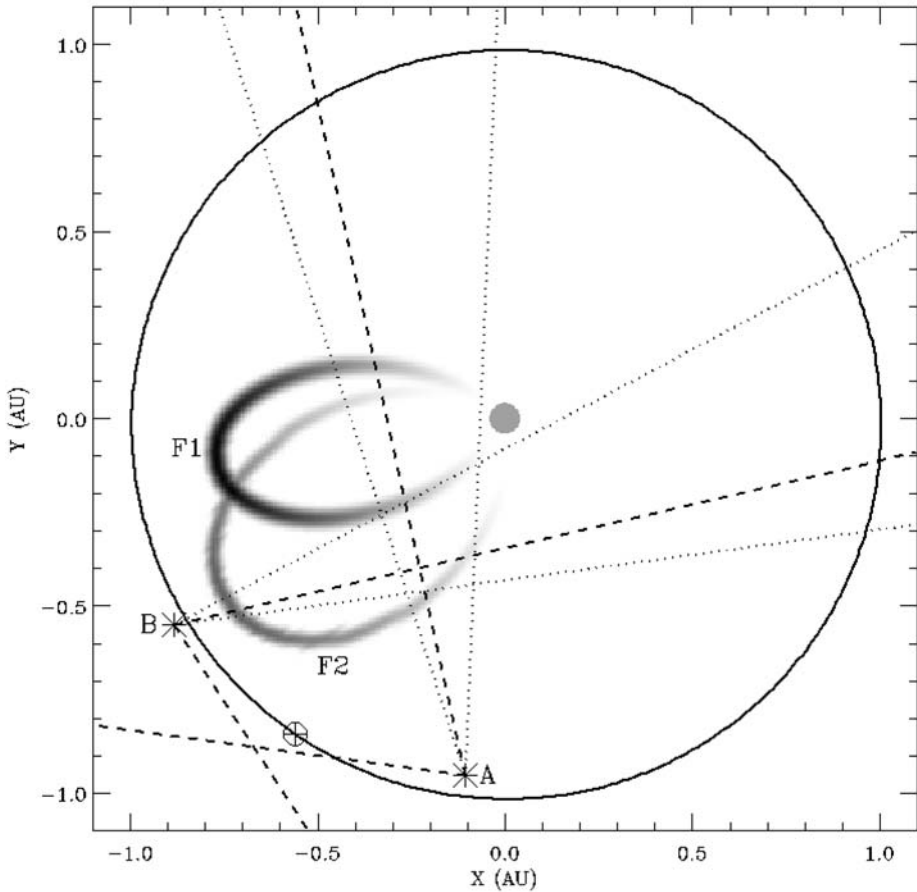
Figure 1 The locations of Earth, STEREO-A, STEREO-B, and the Sun (at the origin) on 17 May 2008 shown in heliocentric aries ecliptic coordinates. Also shown are the locations of the F1 and F2 fronts of the 17 May CME as they approach 1 AU, based on our best 3D reconstruction of the CME morphology (see Section 3). The dotted and dashed lines indicate the fields of view of the HI1 and HI2 telescopes, respectively, onboard STEREO-A and STEREO-B.

from STEREO-B. Closer to Earth, the GOES satellite detects the event as a weak B1.7 flare at 10:05 UT. In EUVI-A He II λ304 images, material is seen lifting off from the flare site after the flare.

Flares and CMEs do not exhibit a one-to-one correspondence (*e.g.*, Harrison, 1996), but in this case there is a white-light CME that follows the flare. This CME is followed by the four white-light imaging telescopes in the SECCHI package from close to the Sun all the way to 1 AU. For a detailed description of SECCHI and its synoptic observing program, see Howard *et al.* (2008). Briefly, SECCHI consists of the aforementioned EUVI coronal imager, two white-light coronagraphs (COR1 and COR2) that collectively observe out to 4.2° (15.6$R_\odot$) from Sun center, and two heliospheric imagers (HI1 and HI2) that monitor the IPM in between the Sun and Earth. Figure 1 explicitly shows the HI1 and HI2 fields of view for both spacecraft, which extend 3.9° – 24.1° and 19° – 89° from the Sun, respectively.
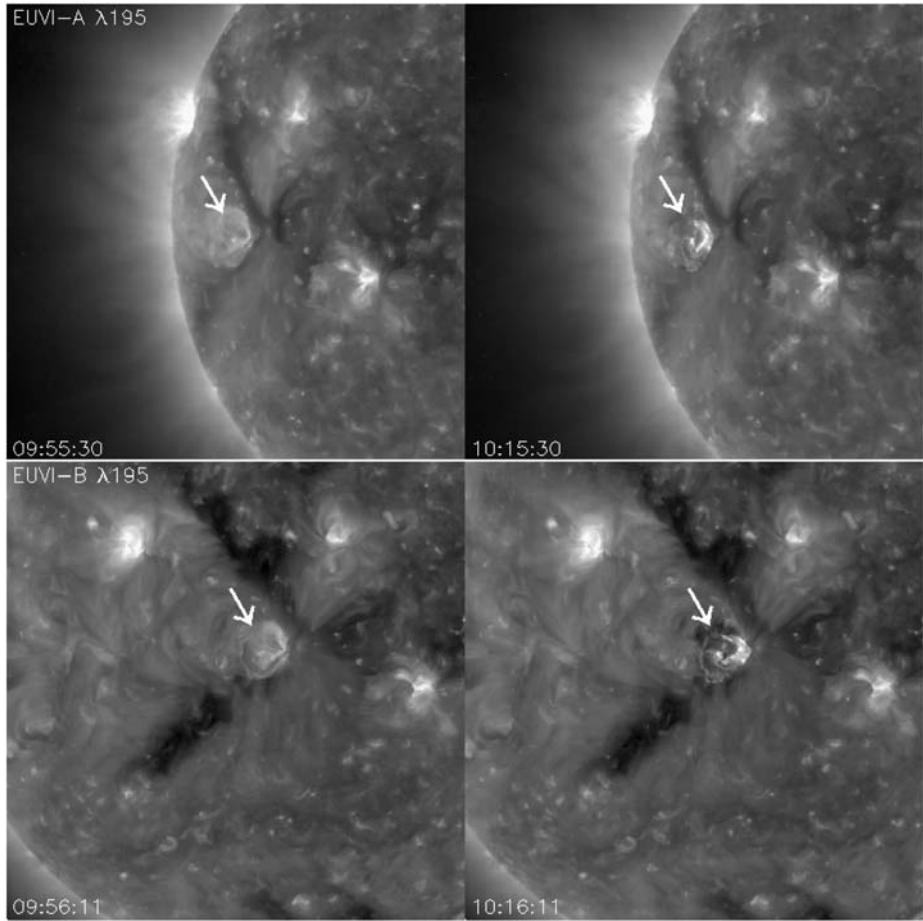
Figure 2 EUVI Fe XII λ195 images of the flare that accompanies the 17 May 2008 CME, where the upper two-image sequence is the view from STEREO-A and the lower two-image sequence is from STEREO-B. The arrows point to the flare site, which is very close to disk center as viewed from STEREO-B.

Figure 3 shows examples of COR2 and HI1 images of the 17 May CME from both spacecraft. These are all running-difference images, where the previous image has been subtracted from each image to emphasize the dynamic CME and de-emphasize static coronal structures. The position of the occulter and the solar outline are indicated in the COR2 images. In the HI1-A image, the Sun is 4° to the right of the field of view, while it is 4° to the left in HI1-B. From the point of view of STEREO-A, the CME expands off the east limb of the Sun, as expected based on the location of the flare. The CME seems to actually consist of two separate fronts, particularly in HI1-A: a bright, narrow front centered close to the ecliptic plane, which we label F1, and a faint, broader front that is centered at a more northern latitude, which we label F2. Our 3D CME reconstruction efforts focus on discerning the intrinsic 3D shape and trajectory of these two fronts. Figure 1 illustrates our conclusions in this regard, and Figures 3 and 4 show synthetic images based on this interpretation, which will be described in detail in the next section.
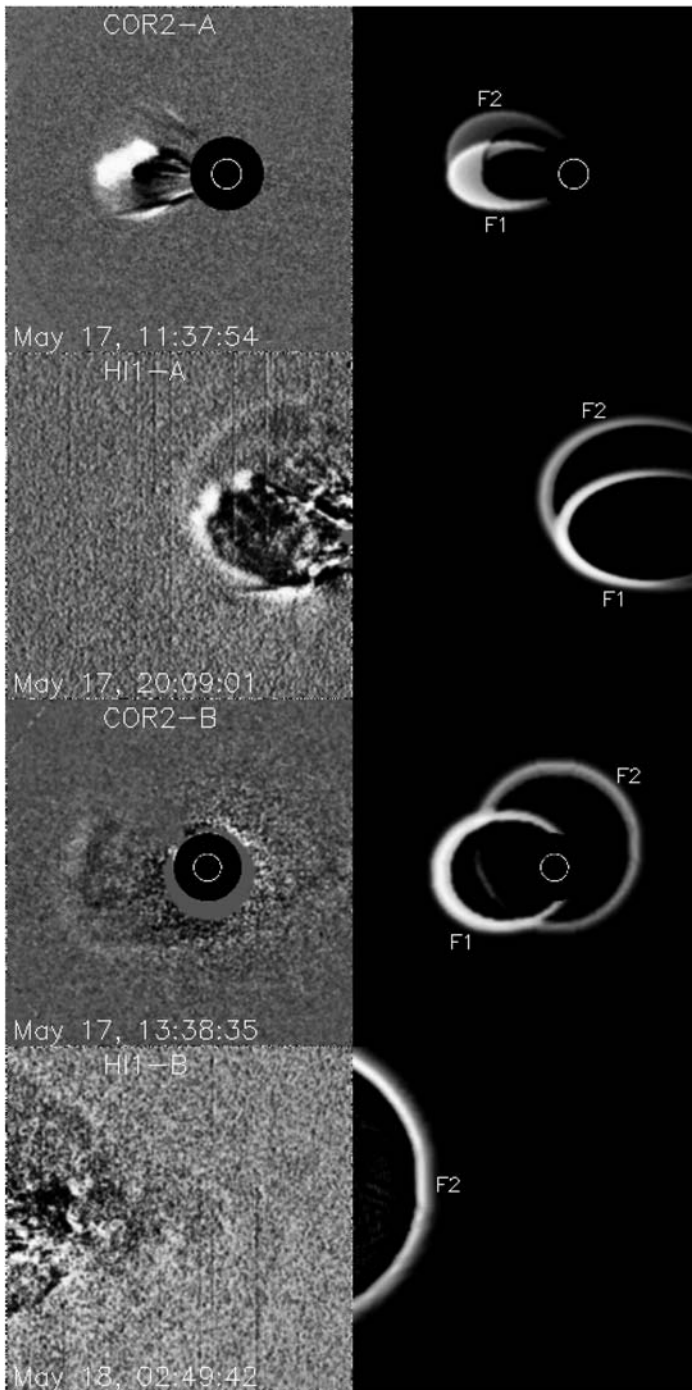
Figure 3 (Left) Examples of COR2-A, HI1-A, COR2-B, and HI1-B images of the 17 May 2008 CME. (Right) Synthetic images of the CME generated from our reconstruction of the 3D mass distribution of the CME, which divides the CME into two separate fronts, F1 and F2 (see Figure 1).
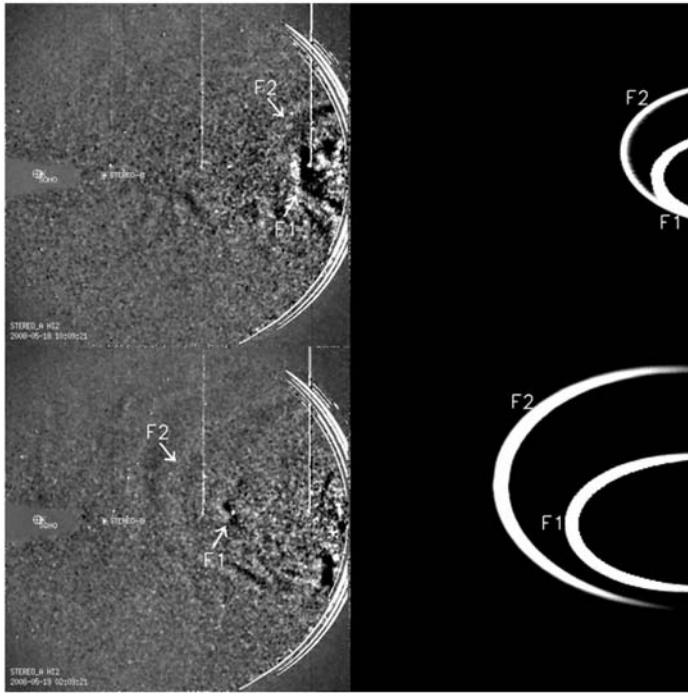
Figure 4 Analogous to Figure 3, this figure compares two HI2-A images of the 17 May CME with synthetic images generated from our 3D model of the event, consisting of two separate fronts, F1 and F2. The locations of Earth, SOHO, and STEREO-B are indicated in the figures. Only part of the F2 front is visible in the first image, and only the tip of the F1 front is detectable in the second.

The disk-center flare location seen by EUVI-B would suggest that the accompanying CME should be directed right at STEREO-B and would therefore predict a full-halo CME from STEREO-B's viewpoint. The COR2-B movies do indeed show a full halo. The western side of the halo is only faintly visible in the COR2-B image in Figure 3, but the west side of the CME is clearly apparent in the HI1-B image. This event is observed as a partial halo event by SOHO (Yashiro *et al.*, 2004). In general, halo CMEs can be either back-side or front-side events, but the flare location and the relative appearance of the CME as seen from STEREO-A and STEREO-B clearly indicate a front-side event in this case.

Moving to HI2, Figure 4 shows two HI2-A images of the CME and also indicates the locations of Earth, SOHO, and STEREO-B in the field of view. The brightness of CMEs naturally decreases with distance from the Sun, and CME fronts are as a consequence typically quite faint in the HI2 field of view. The issue of CME brightness is dealt with in more detail by Vourlidas and Howard (2006). The situation is further complicated by the complex background of stars, planets, and Milky Way in the huge HI2 field of view, which must be subtracted. The initial HI2 image-processing procedure is described by Sheeley *et al.* (2008). Although the F1 and F2 fronts of the 17 May CME can be followed in HI2-A movies, it is frustratingly difficult to make them visible in single frames, and extensive experimentation with different scalings and contrast levels was required to produce the images in Figure 4. In the first image (at 10:09 UT on 18 May), F1 is seen shortly after entering the field of view and is still fairly bright, but only the northern part of F2 can really be seen. By the second image (at 2:09 UT on 19 May), F1 has faded and only the tip of the front can still be clearly

seen. In contrast, the full F2 front can now be seen, albeit very faintly. Finally, we note that there is only a hint of the CME's presence in HI2-B images, so we do not try to show HI2-B data here.

3. Modeling the 3D Density Distribution

In trying to reconstruct the shape and orientation of the F1 and F2 fronts, it is useful to have some parametrized form for the fronts, to make it easier to experiment with different shapes in a predictable and reproducible fashion. We start by defining a profile using the following equation in polar coordinates:

$$r(\theta) = r_{\max} \exp\left(-\frac{1}{2}\left|\frac{\theta}{\sigma}\right|^{\alpha}\right). \tag{1}$$

This creates a two-dimensional loop, where $r_{\max}$ is the maximum radius of the shape, the σ parameter determines its width, and α changes its shape. For $\alpha = 2$, Equation (1) is just the equation for a Gaussian, and $r(\theta)$ can be referred to as a polar Gaussian. Higher values of α result in loops with flatter tops.

Although the loop is initially created in polar coordinates, we immediately shift to Cartesian coordinates for the next step, which is to use the loop to map densities onto a two-dimensional plane. It is Thomson scattering of electrons that determines brightness in white-light CME images, so it is electron density in particular that we are interested in. We assume a Gaussian density profile across the loop, such that if we define $\delta(x, y)$ as the distance to the loop from a point (x, y) in the xy-plane, then the density map is

$$n_1(x, y) = n_{\max} \exp\left[-\frac{1}{2}\left(\frac{\delta(x, y)}{\sigma_n}\right)^2\right]. \tag{2}$$

This creates an even density distribution along the loop with maximum density $n_{\max}$. The σ_n parameter defines the width of the density profile across the loop. In Cartesian coordinates, the loop is symmetric about the x-axis. We allow for an x dependence of density by computing a final density map using

$$n_2(x, y) = n_1(x, y)\left(\frac{x}{r_{\max}}\right)^{\beta}. \tag{3}$$

For $\beta > 0$, densities will increase with distance from the Sun, whereas for $\beta < 0$ they will decrease. Finally, we rotate the $n_2(x, y)$ density distribution about the x-axis to obtain our final three-dimensional density cube containing the front, $n_3(x, y, z)$. This generates a density cube with a 3D front that is azimuthally symmetric about the x-axis.

The final step is to rotate the front to the desired direction. We do so in an HAE coordinate system, like the one shown in Figure 1. The rotation direction is defined by an azimuthal longitude, l_F, within the xy-plane shown in the figure, where $l_F = 0°$ is in the direction of the positive x-axis, and we define a poloidal latitude, b_F, to be the angle out of the xy-plane. So (l_F, b_F) indicates the direction where the x-axis of the original $n_3(x, y, z)$ density cube ends up pointing.

All told there are eight parameters that are used to model the 3D shape of a CME front: $r_{\max}, \sigma, \alpha, n_{\max}, \sigma_n, \beta, l_F,$ and b_F. Separate sets of parameters are used to create the F1 and F2 fronts, which are then combined into a single density cube. This cube is then inserted

Table 1 Front parameters.

Quantity	F1	F2
r_{max}	1	1.17
σ (degrees)	25.5	31.9
α	2	2
n_{max}	1	0.12
σ_n	0.0149	0.0119
β	3	3
l_F (degrees)	188	213
b_F (degrees)	−2	8

into a white-light rendering routine (Thernisien, Howard, and Vourlidas, 2006) to produce synthetic SECCHI images for comparison with the real ones. The visibility of CMEs in white-light images relies on Thomson scattering of solar photons by electrons in the CME, and the white-light renderer properly considers the Thomson scattering angles in deriving the synthetic images (Billings, 1966).

One of the most important assumptions made in this whole analysis is that CMEs expand in a self-similar fashion, meaning that they maintain the same shape as they expand. With this assumption a single density cube can be used to represent the mass distribution of a CME at all times, and therefore we can try to reproduce the CME appearance in the COR1, COR2, HI1, and HI2 fields of view using the same density cube. The only thing that changes as a function of time are the axis scales of the cube. We rely on the kinematic analysis described in Section 5 to provide the proper expansion factors for the axes as a function of time.

Ideally, there would be some way to properly quantify how well a density cube reproduces the SECCHI data. If this were possible, we could perhaps automate the variation of input parameters to numerically converge on a best fit. But this is not practical, because the data-model comparison is being done for all SECCHI images of the CME simultaneously (well over a hundred total), using data from both STEREO spacecraft. Thus, subjective human judgment is relied on to assess the quality of fit, by comparing movies of the actual and synthetic CME images. Simple trial and error is used to adjust the parameters to find the model that seems to work best.

Table 1 lists the F1 and F2 parameters that represent our best effort at reproducing the 17 May CME morphology. It should be noted at this point that the treatment of densities is of secondary importance in this particular analysis, since we are focused on assessing the shape and orientation of the 17 May CME fronts, and we are *not* attempting to reproduce the absolute CME brightness observed by SECCHI. Thus, the n_{max}, σ_n, and β parameters listed in Table 1 are of limited validity, and in fact n_{max} of the F1 front is simply normalized to 1. If we were to try to reproduce CME brightness, it would clearly be necessary not only to work with absolute density values but also to add some time dependence to account for their decrease as the CME expands outward. The r_{max} parameter of F1 is also normalized to 1, since there is no absolute distance scale associated with the density cube until the expansion factors provided by the kinematic analysis are taken into account. For both n_{max} and r_{max} it is only the relative values of these quantities for the F1 and F2 fronts that matter. The σ_n parameter is quoted in the same normalized distance units as r_{max}.

Figure 1 shows a slice through the ecliptic plane of our best 3D model of the 17 May CME, indicating the shape and orientation of the F1 and F2 fronts as they approach 1 AU. Figures 3 and 4 show synthetic images of the CME, paired with the SECCHI images they are meant to reproduce. The synthetic images are displayed in running-difference mode like

the real images. We find that our model is reasonably successful in reproducing the general appearance of the 17 May CME.

Our analysis places F1 in the background and F2 in the foreground as viewed from STEREO-A. The primary visual evidence for this is that the F1 front exhibits an apparent deceleration in the IPM not exhibited by F2, particularly in HI2-A. This leads to F2 gradually moving further and further ahead of F1 with time in the HI1-A and HI2-A images (see Figures 3 and 4). Sheeley *et al.* (2008) and Rouillard *et al.* (2008) have discussed how apparent decelerations and accelerations in HI images can be indicative of the trajectory of a front. This is why the HI2-A data are very helpful in our analysis, despite the faintness of the fronts. The F1 front decelerates through HI2-A, and it also fades greatly owing to its trajectory carrying it further away from the viewer and away from the "Thomson sphere" (Vourlidas and Howard, 2006). The F1 front disappears before reaching the apparent location of STEREO-B, whereas the F2 front can actually be followed all the way through the field of view. As suggested by Figure 1, this can be explained by F2 traveling in the foreground across the line of sight in the HI2-A field of view, while F1 in the background appears to decelerate because of the component of its motion away from STEREO-A. The COR2-B data provide further support for this geometry, as they show that the brightest part of the CME, which is naturally associated with the brighter F1 front, is the westernmost part. While we orient F1 only a couple of degrees south of the ecliptic, F2 is 8° north of it. The latitudinal orientation is best discerned visually in the COR2-B synthetic image.

4. *In Situ* Observations

Based on the flare's location very close to disk center as seen from STEREO-B (see Figure 2), the initial expectation would be that the CME should be directed right at STEREO-B, if radial expansion from the flare site is assumed. However, our 3D reconstruction implies that the F1 front that contains most of the CME's mass is directed west of STEREO-B and ends up missing STEREO-B entirely (see Figure 1). The reconstruction suggests that STEREO-B is struck instead by the weaker, fainter F2 front, which unlike F1 *does* travel in roughly the direction that the flare site would predict.

There are two *in situ* instruments onboard both STEREO spacecraft that can be used to study CMEs that happen to strike the spacecraft: the Plasma and Suprathermal Ion Composition (PLASTIC) instrument (Galvin *et al.*, 2008) and the In-situ Measurements of Particles and CME Transients (IMPACT) experiment (Acuña *et al.*, 2008; Luhmann *et al.*, 2008). The former provides measurements of proton densities and velocities; the latter provides magnetic field measurements. Figure 5 shows PLASTIC-B and IMPACT-B measurements from 19 May. The dashed line indicates the predicted arrival time of the F2 front (see Section 5). There is indeed a brief density enhancement at the predicted time, accompanied by a magnetic field enhancement and a jump in wind velocity from 540 to 600 km s^{-1}.

This apparent *in situ* signature of the F2 front is rather weak, and by itself it is not indicative of the passage of an interplanetary CME (ICME). There is no rotation of the magnetic field vector or bidirectional heat fluxes in the IMPACT data, and there is no extended period of low plasma beta or temperature in the PLASTIC data. Signatures of ICMEs can vary significantly from one event to another (*e.g.*, Jian *et al.*, 2006), but this *in situ* signature looks more like that of a corotating interaction region (CIR), where high-speed wind is running into low-speed wind in the IPM. Complicating the situation further is that there is strong evidence that there is in fact a CIR passing by at this time. Close inspection of HI2-A movies shows faint fronts in the field of view that are likely CIR components. The gradual
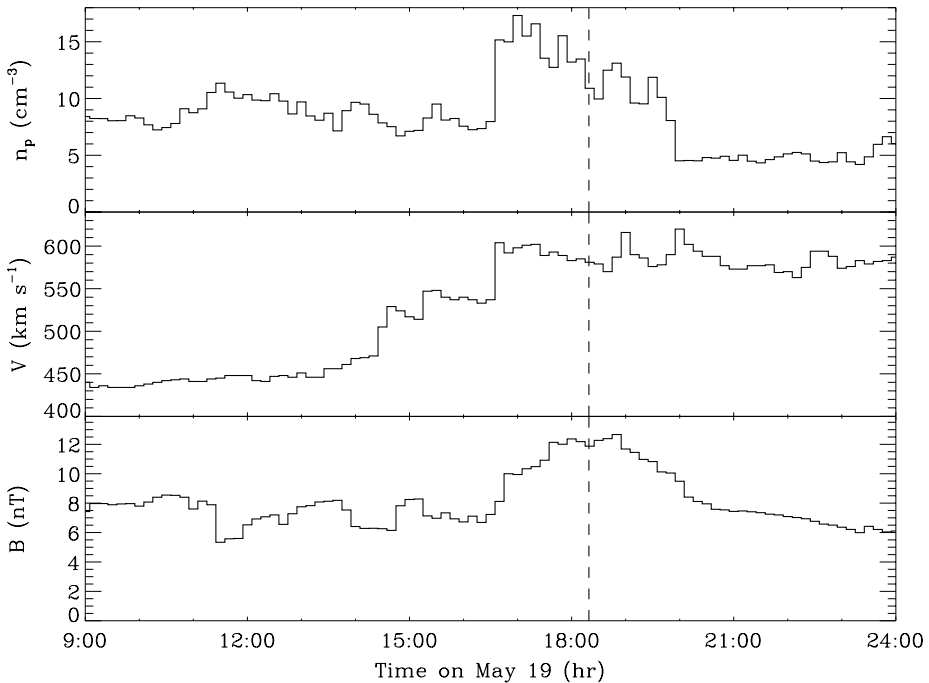
Figure 5 *In situ* measurements of the 17 May CME observed at STEREO-B, which hits the spacecraft at about 16:30 UT on 19 May. The upper two panels are the proton density and velocity measurements from the PLASTIC instrument, and the bottom panel is the magnetic field measurement from IMPACT. The dashed line is the arrival time of the F2 front of the CME predicted by the kinematic model in Section 5.

increase in wind speed seen in Figure 5 is indicative of a CIR passage. This increase is seen in SOHO/CELIAS data the following day, and in PLASTIC-A on 21 May, illustrating the effects of solar rotation on the CIR, which leads the CIR to first pass over STEREO-B on 19 May, then Earth (and spacecraft at L1) on 20 May, and finally STEREO-A on 21 May. Finally, Figure 2 shows that there are low-latitude coronal holes near the flare site, which are likely sources of the high-speed wind creating this CIR.

Nevertheless, our ability to follow the F2 front continuously from close to the Sun to 1 AU in about two days leads us to conclude that this is part of the 17 May CME and not a CIR, as CIR fronts are simply not observable very close to the Sun like F2 is. Furthermore, the perfect coincidence between the predicted F2 arrival time and the narrow density peak in Figure 5 leads us to still conclude that this is likely the *in situ* signature of F2, even though it is likely that F2 is in some sense embedded in a CIR structure moving by at about the same time. The CIR signature seen by STEREO-A on 21 May shows a strong density and magnetic field enhancement, unlike anything seen on 19 May by STEREO-B. Perhaps the 17 May CME's F2 front could in fact be responsible for muddling the CIR structure near STEREO-B. It is also possible that the F2 front has been affected by interaction with the CIR. There is evidence of a small-scale flux rope about six hours after the main density peak. Perhaps this is the magnetic driver of the F2 front, and perhaps the high speed of the CME led to a CME–CIR interaction whereby the CME may have caught up with the CIR.

It is worth emphasizing that the core of the 17 May CME is probably represented by the brighter, denser F1 front, which misses STEREO-B entirely. Although our 3D reconstruction

is not meant to precisely assess densities (see Section 3), we note that in our model it is assumed that F2 has a density only 12% that of F1 (see Table 1), an assumption meant to account for the faintness of F2 relative to F1. If F1 had hit STEREO-B instead of F2, possibly a more conventional *in situ* ICME signature would have been seen. Perhaps the F2 front is a shock or CIR-like front launched by F1's interaction with the ambient solar wind. In any case, the F2 front seems to be a peripheral part of the CME rather than a central part, and the apparent F2 signature in Figure 5 should be considered with that in mind.

5. Kinematic Model

As already mentioned, our 3D reconstruction requires a kinematic model of the CME to provide expansion factors for the density cube as a function of time. The STEREO-A observations are much more useful than those of STEREO-B for these purposes, as STEREO-A's lateral view of the CME provides a much better perspective for tracking the CME's leading edge over time. We focus our attention on the F1 front, as it is generally much easier to track than F2, the exception being at later times in the HI2-A field of view when F2 actually becomes somewhat brighter. The elongation angle, ϵ, of the F1 leading edge is measured as a function of time. These elongation angles are converted to actual Sun-center distances, r, using the following equation (Kahler and Webb, 2007; Sheeley *et al.*, 2008; Wood *et al.*, 2009):

$$r = \frac{d \sin \epsilon}{\sin(\epsilon + \phi)}, \qquad (4)$$

where d is the distance to STEREO-A from the Sun, which is just under 1 AU (see Figure 1). The angle ϕ is the angle between the CME trajectory and STEREO-A's line of sight to the Sun. Our best model from Section 3 implies $\phi = 77°$ for F1 as viewed from STEREO-A.

The top panel of Figure 6 shows the resulting distance measurements as a function of time. We fit these data points with a simple kinematic model that we have used recently (Wood *et al.*, 2009), in which we assume an initial acceleration for the CME, a_1, persisting until a time t_1, followed by a second acceleration (or deceleration), a_2, lasting until time t_2, followed finally by constant velocity. Assuming 1%, 2%, and 3% error bars for the COR1/COR2, HI1, and HI2 distance measurements, respectively, we use a χ^2 minimization routine to establish the best-fit parameters (Bevington and Robinson, 1992). The solid line fitted to the data in the top panel of Figure 6 is the resulting fit, and the solid lines in the lower two panels indicate the velocity and acceleration profiles implied by this fit.

The model suggests an initial acceleration of $a_1 = 240$ m s^{-2}, but this measurement must be considered with skepticism considering that there are only two data points that cover this initial acceleration period. Even if one accepts the weak evidence for acceleration at all, with so few data points it is surely not possible to measure it very precisely. In any case, the CME has already reached its peak velocity of 1009 km s^{-1} midway through the COR1 field of view, less than $3R_\odot$ from Sun center. At solar minimum, events over 1000 km s^{-1} like this one are less common than at more active times (Yashiro *et al.*, 2004). The CME gradually decelerates at a rate of $a_2 = -11.0$ m s^{-2} through COR2 and into the HI1 field of view, with the deceleration stopping at a velocity of 774 km s^{-1}. The high initial speed and the measurable deceleration in the IPM place this CME in the second category described by Sheeley *et al.* (1999).

It is worthwhile to compare our results with those of Thernisien, Vourlidas, and Howard (2009), who have analyzed the velocity and trajectory of the 17 May CME using a flux-rope
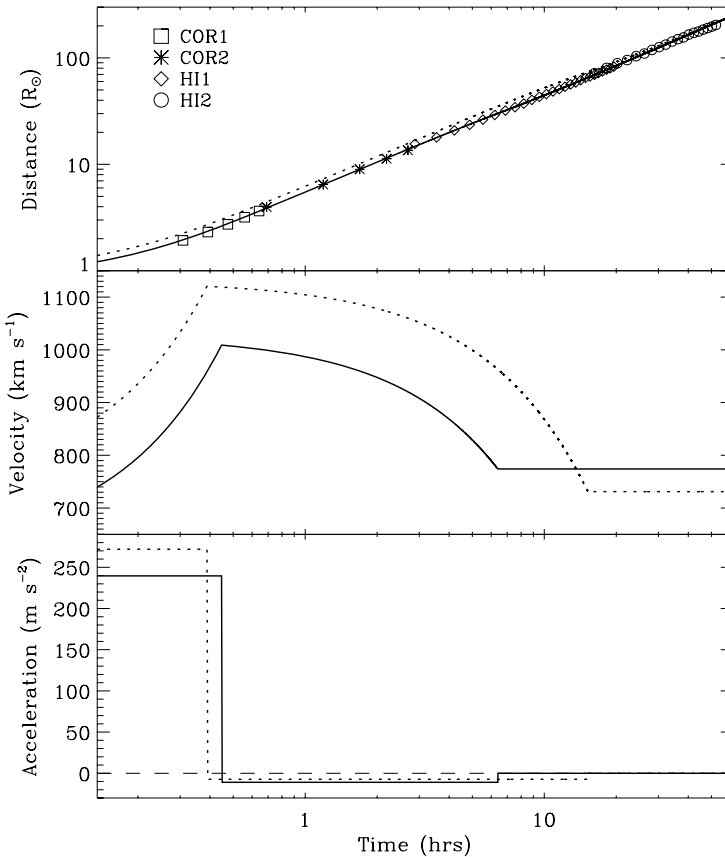
Figure 6 (Top) The distance from Sun center of the leading edge of the F1 component of the 17 May 2008 CME as a function of time. The solid line is a fit to these data points based on a simple kinematic model assuming an initial acceleration phase, a second deceleration phase, and then a constant velocity phase. The dotted line is a similar fit that results from measurements of the F2 front of the CME. (Middle) The velocity and (bottom) acceleration profiles suggested by the F1 and F2 fits (solid and dotted lines, respectively).

fitting procedure. They find a trajectory (in HAE coordinates) of $(l_F, b_F) = (191°, -13°)$, and they measure a velocity of $V = 986$ km s^{-1} for the CME in the COR2 field of view. These measurements agree well with our measurements of the F1 front of the CME: $(l_F, b_F) = (188°, -2°)$ from Table 1 and an average COR2 velocity of $V = 959$ km s^{-1}. Since Thernisien, Vourlidas, and Howard (2009) focus only on COR2 data, where the F1 front is much brighter and more apparent than F2 (see Figure 3), it is not surprising that this is the part of the CME that has been quantified.

If we assume that interaction with the ambient solar wind is responsible for the CME's IPM deceleration (Cargill, 2004; Tappin, 2006), the halting of the deceleration with the CME still at a speed as high as 774 km s^{-1} implies that the CME is expanding into a solar wind that is faster than the canonical ~400 km s^{-1}. The *in situ* data provide support for this interpretation. The solar wind seen by STEREO-B after the CME passes by is high speed (~600 km s^{-1}) wind (see Figure 5), and these high velocities persist for many days afterward. Most studies of high-speed wind suggest that most of its acceleration happens close to the Sun, probably within the COR2 field of view (Grall *et al.*, 1996;

Kojima *et al.*, 2004). Thus, this high-speed wind is presumably indicative of the ambient wind speed seen by the CME for most of its journey to 1 AU. As a consequence of its high speed, the CME takes only a little over two days to make it from the Sun to 1 AU. Most of the deceleration of the CME happens relatively close to the Sun, well before the CME reaches the HI2 field of view. This is consistent with our previous analysis of a 4 February 2008 CME (Wood *et al.*, 2009), and with studies of CME speeds using interplanetary scintillation measurements (Jones *et al.*, 2007).

Figure 6 also shows the distance, velocity, and acceleration profiles that we derive for the F2 front using the same analysis performed for F1. In our 3D reconstruction from Section 3, we assumed that the entire CME structure expands in a self-similar fashion. Our best fit suggested that F2 is 1.17 times larger than F1 (see Table 1). For self-similar expansion to be strictly true, this would mean that F2 is *always* 1.17 times larger than F1 and that its velocity and acceleration are also *always* 1.17 times larger than those of F1.

The reasonable level of success that we had with our 3D reconstruction in Section 3 implies that self-similar expansion is not a bad first-order assumption, but the kinematic analysis illustrates its limitations. Figure 6 shows deviations from self-similar expansion, since the dotted lines are *not* always the same multiple of the solid lines at all times, particularly at later times in the HI2-A field of view, when the F2 velocity falls below that of F1 and the F1 distance ultimately catches up with F2. Careful comparison of the real and synthetic HI2-A images (as in Figure 4) shows that the 3D model (under the assumption of self-similar expansion) predicts too much separation between the F1 and F2 fronts at later times in the HI2-A field of view, an effect that is beginning to become apparent at the time of the second HI2-A image in Figure 4.

In any case, it is the kinematic model of the F2 front in Figure 6 that provides the best estimate for when the CME is expected to hit STEREO-B, better than the self-similarly expanding 3D model in Section 3 – though it is that model that provides the kinematic analysis with the trajectory information necessary to compute distances from elongation angles and discern what part of the CME actually hits the spacecraft. The F2 kinematic model indicates a total travel time of 56.6 hours to STEREO-B, arriving at 18:19 UT on 19 May. This agrees beautifully with the timing of the weak PLASTIC and IMPACT CME signature seen in Figure 5.

6. Geometric Corrections for CME Elongation Angle Measurements

The kinematic analysis in the previous section requires measuring the elongation angle of the CME leading edge as a function of time. One systematic error that has not yet been mentioned with regards to these measurements is that the apparent leading edge seen from a given vantage point may not be the real leading edge. Furthermore, the location of the apparent leading edge along a CME front can actually change as the CME expands outward and the viewing angle changes. This is illustrated in the left panel of Figure 7, which shows a geometry very much like that of STEREO-A's view of the F1 front of the 17 May CME. The dashed line indicates the line of sight from the observer (STEREO-A) to the real leading edge, but the dotted line shows the line of sight to the apparent leading edge. The difference between the two means that the leading edge distance computed using Equation (4), indicated by a square in the figure, will overestimate the actual leading edge distance, indicated by a diamond. By experimenting with different expansion factors for the CME front, we can determine how this discrepancy changes with elongation angle. The right half of Figure 7 shows the ratio of real to measured distance as a function of measured elongation angle, for this particular CME front shape and viewing geometry.
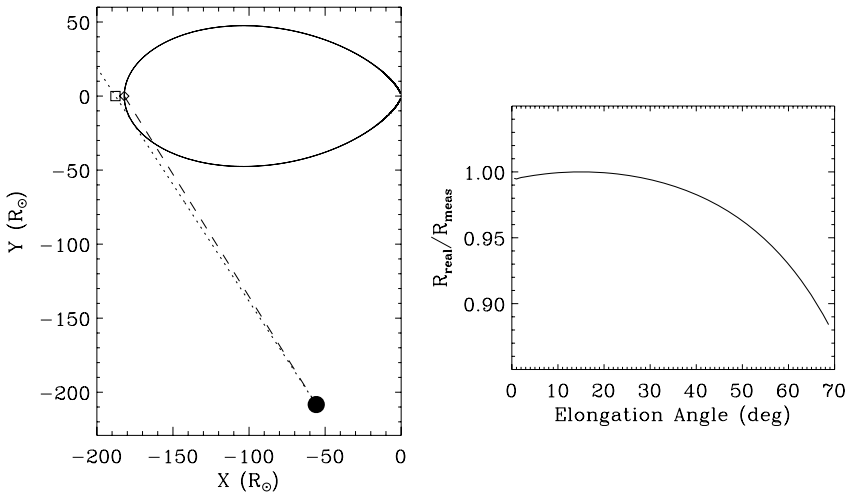
Figure 7 In the left panel, the solid line is a model CME front, and the filled circle represents the vantage point of an observer of the CME. This geometry is meant to be very similar to STEREO-A's view of the F1 front of the 17 May 2008 CME (see Figure 1). The dashed line is the line of sight from the observer to the real leading edge of the CME (diamond); the dotted line is the line of sight to the apparent leading edge seen by the observer. The square indicates where the observer will think the leading edge is if Equation (4) is used. By experimenting with different expansion factors for this model CME shape, the right panel shows the ratio of real to measured leading edge distance as a function of measured elongation angle for this particular CME shape and viewing geometry.

This problem could potentially lead to large errors (>25%) in the CME velocities and accelerations inferred from any kinematic analysis, depending on the exact geometry of the situation. Without knowing the actual CME shape, little can be done to correct for this systematic uncertainty. But the 3D reconstruction procedure in Section 3 has given us an estimate of the CME front geometry. This allows us to perform experiments like that in Figure 7, which provides correction factors to apply to measured elongation angles to convert them to elongation angles of the *real* leading edge. This correction was actually performed in the kinematic analysis discussed in the previous section, and the distances shown in Figure 6 are corrected for this geometric effect. For this particular CME we do not find that the corrections result in any dramatic change to any quantities of interest (<5% for velocities), but the geometric corrections could end up being more important for other CMEs and viewing angles.

One final clarification must be made with regards to the whole analysis process. In Section 3, we noted that the kinematic analysis is needed by the 3D reconstruction procedure to provide expansion factors for the density cube, whereas in Section 5 and here in Section 6 we note that the 3D reconstruction results are needed in the kinematic analysis to provide CME front trajectories and the geometric corrections described in this section. So which comes first, the kinematic analysis or the 3D reconstruction? In practice, it is necessary to iterate between the two to ultimately converge on a final self-consistent solution. Thus, this whole analysis does have the disadvantage of being rather time consuming.

7. Summary

We have here described an intuitive method for reconstructing the 3D mass distribution of CMEs extensively observed by the SECCHI imagers on STEREO, and we have applied this method to modeling the morphology of the 17 May 2008 CME. We find that the CME's basic appearance can be reproduced all the way from near the Sun to 1 AU by modeling the CME as a superposition of two overlapping fronts, labeled F1 and F2, expanding in a self-similar fashion. The F1 front is smaller and directed westward of the trajectory that the flare site would have predicted (under the assumption of purely radial expansion), but this front contains most of the mass of the CME. The F2 front is broader but fainter, and it *does* expand roughly in the direction implied by the flare site, which ultimately leads the front to hit STEREO-B on 19 May. It is uncertain what the two-component nature of the CME implies about the underlying magnetic structure. There is evidence for a small flux rope following the F2 front, but the true core of the CME may actually lie within the brighter F1 front. The faintness of F2 makes it appear like merely a peripheral part of the CME, which is possibly influenced by the presence of a CIR.

The 17 May CME is an unusually fast CME for solar minimum conditions, with the F2 front reaching speeds up to $1120 \, \text{km s}^{-1}$. The CME decelerates on its way to 1 AU, but this deceleration stops while the CME velocity is still above $700 \, \text{km s}^{-1}$. As a consequence, the CME takes only a little over 2 days to reach 1 AU. The sustained high speed of the CME may be due to expansion into high-speed solar wind, which would naturally limit the drag between the CME and ambient wind.

Our kinematic model of the F2 front, guided by the 3D reconstruction, provides a precise prediction for when the CME should hit STEREO-B, and PLASTIC and IMPACT data show that there is indeed a weak density, velocity, and magnetic field enhancement at that time that we interpret as the CME signature. This illustrates one big advantage of SECCHI's ability to follow a CME front continuously to 1 AU: If the CME hits a spacecraft one can potentially identify signatures of the CME in *in situ* data that would otherwise be too weak for anyone to associate the signature with a CME. The 3D reconstruction provides a simple explanation for the weakness of the signature, namely that STEREO-B is hit by the faint F2 front instead of by the F1 front containing most of the CME's mass.

References

Acuña, M.H., Curtis, D., Scheifele, J.L., Russell, C.T., Schroeder, P., Szabó, A., Luhmann, J.G.: 2008, *Space Sci. Rev.* **136**, 203.
Antunes, A., Thernisien, A., Yahil, A.: 2009, *Solar Phys.* in press.
Antunes, A., Cook, J.W., Newmark, J.S., Ontiveros, V., Thernisien, A.: 2008, *Eos Trans. AGU* **89**(23), Jt. Assem. Suppl., Abstract SH21A-07.
Bevington, P.R., Robinson, D.K.: 1992, *Data Reduction and Error Analysis for the Physical Sciences*, McGraw-Hill, New York.
Billings, D.E.: 1966, *A Guide to the Solar Corona*, Academic Press, New York.
Cargill, P.J.: 2004, *Solar Phys.* **121**, 135.
Chen, J., Howard, R.A., Brueckner, G.E., Santoro, R., Krall, J., Paswaters, S.E., St. Cyr, O.C., Schwenn, R., Lamy, P., Simnett, G.M.: 1997, *Astrophys. J.* **490**, L191.

Galvin, A.B., Kistler, L.M., Popecki, M.A., Farrugia, C.J., Simunac, K.D.C., Ellis, L., Möbius, E., Lee, M.A., Boehm, M., Carroll, J., *et al.*: 2008, *Space Sci. Rev.* **136**, 437.

Gibson, S.E., Low, B.C.: 1998, *Astrophys. J.* **493**, 460.

Grall, R.R., Coles, W.A., Klinglesmith, M.T., Breen, A.R., Williams, P.J.S., Markkanen, J., Esser, R.: 1996, *Nature* **379**, 429.

Harrison, R.A.: 1996, *Solar Phys.* **166**, 441.

Harrison, R.A., Davis, C.J., Eyles, C.J., Bewsher, D., Crothers, S.R., Davies, J.A., Howard, R.A., Moses, D.J., Socker, D.G., Newmark, J.S., *et al.*: 2008, *Solar Phys.* **247**, 171.

Howard, R.A., Moses, J.D., Vourlidas, A., Newmark, J.S., Socker, D.G., Plunkett, S.P., Korendyke, C.M., Cook, J.W., Hurley, A., Davila, J.M., *et al.*: 2008, *Space Sci. Rev.* **136**, 67.

Jian, L., Russell, C.T., Luhmann, J.G., Skoug, R.M.: 2006, *Solar Phys.* **239**, 393.

Jones, R.A., Breen, A.R., Fallows, R.A., Canals, A., Bisi, M.M., Lawrence, G.: 2007, *J. Geophys. Res.* **112**, A08107.

Kahler, S.W., Webb, D.F.: 2007, *J. Geophys. Res.* **112**, A09103.

Kojima, M., Breen, A.R., Fujiki, K., Hayashi, K., Ohmi, T., Tokumaru, M.: 2004, *J. Geophys. Res.* **109**, A04103.

Krall, J.: 2007, *Astrophys. J.* **657**, 559.

Luhmann, J.G., Curtis, D.W., Schroeder, P., McCauley, J., Lin, R.P., Larson, D.E., Bale, S.D., Sauvaud, J.-A., Aoustin, C., Mewaldt, R.A., *et al.*: 2008, *Space Sci. Rev.* **136**, 117.

Manchester, W.B., Gombosi, T.I., Roussev, I., De Zeeuw, D.L., Sokolov, I.V., Powell, K.G., Tóth, G., Opher, M.: 2004, *J. Geophys. Res.* **109**, A01102.

Rouillard, A.P., Davies, J.A., Forsyth, R.J., Rees, A., Davis, C.J., Harrison, R.A., Lockwood, M., Bewsher, D., Crothers, S.R., Eyles, C.J., *et al.*: 2008, *Geophys. Res. Lett.* **35**, L10110.

Sheeley, N.R. Jr., Walters, J.H., Wang, Y.-M., Howard, R.A.: 1999, *J. Geophys. Res.* **104**, 24739.

Sheeley, N.R. Jr., Herbst, A.D., Palatchi, C.A., Wang, Y.-M., Howard, R.A., Moses, J.D., Vourlidas, A., Newmark, J.S., Socker, D.G., Plunkett, S.P., *et al.*: 2008, *Astrophys. J.* **675**, 853.

Tappin, S.J.: 2006, *Solar Phys.* **233**, 233.

Thernisien, A.F.R., Howard, R.A., Vourlidas, A.: 2006, *Astrophys. J.* **652**, 763.

Thernisien, A., Vourlidas, A., Howard, R.A.: 2009, *Solar Phys.* **256**, 111.

Vourlidas, A., Howard, R.A.: 2006, *Astrophys. J.* **642**, 1216.

Wood, B.E., Howard, R.A., Plunkett, S.P., Socker, D.G.: 2009, *Astrophys. J.* **694**, 707.

Wu, S.T., Andrews, M.D., Plunkett, S.P.: 2001, *Space Sci. Rev.* **95**, 191.

Yashiro, S., Gopalswamy, N., Michalek, G., St. Cyr, O.C., Plunkett, S.P., Rich, N.B., Howard, R.A.: 2004, *J. Geophys. Res.* **109**, A07105.